Journal of Energy Storage 162 (2026) 122025

Contents lists available at ScienceDirect

Journal of Energy Storage

journal homepage: www.elsevier.com/locate/est

Research papers

# Aza-Anthraquinone derivative as a highly stable negolyte for acidic aqueous organic flow batteries

Qiujun Li [a,b,1], Maxime Artault [c,1], Chanez Maouche [a,b,1,*], Gabriel Gonzalez [a], Petri M. Pihko [c,**], Pekka Peljo [a,b,*]

[a] Research group of Battery Materials and Technologies, Department of Mechanical and Materials Engineering, University of Turku, 20014, Turku, Finland
[b] Department of Chemistry and Materials Science, Aalto University, 02150, Espoo, Finland
[c] Department of Chemistry and NanoScience Centre, University of Jyväskylä, 40014, Jyväskylä, Finland

ARTICLE INFO

*Keywords:*
Aqueous organic flow batteries
Aza-anthraquinone
High solubility
Long-duration energy storage

ABSTRACT

Aqueous organic flow batteries (AOFBs) offer a scalable pathway for long-duration energy storage, yet their performance is often limited by the solubility, stability, or kinetic behavior of organic redox materials. We report a molecular design strategy based on the *N*-alkylation of 5,8-difluoro-2-aza-anthraquinone to access a new class of quaternized pyridinium salts (AAQ-1, AAQ-2, AAQ-3). *N*-alkylation of the pyridinium group enhanced solubility and enabled the tuning of redox behavior. AAQ-1 displayed superior electrochemical characteristics, including high solubility (847 mM in 2 M $H_2SO_4$) and fast charge transfer kinetics ($k^0 = 2.6 \times 10^{-2}$ cm/s). Full-cell tests at both low and high concentrations further demonstrated very good stability, with a small capacity fade of 0.05% per day at high concentration, reaching a volumetric capacity of 25.6 Ah/L and a theoretical maximum of 43.4 Ah/L. AAQ-3 showed stable cycling at low concentration with small capacity decay of 0.46% per day. Post-mortem analyses on AAQ-1 revealed no structural degradation. Additionally, Pourbaix analysis confirmed a $2e^-/2H^+$ proton-coupled electron transfer mechanism active under acidic conditions. This work introduces a practical, scalable, and tuneable redox platform for AOFBs. Through functional design, we demonstrate the feasibility of high-performance organic negolytes for long-duration, sustainable energy storage systems.

## 1. Introduction

The development of energy storage devices with high density, high safety and cost-efficiency is critical for efficient utilization of intermittent renewable energy resources such as solar, wind and hydropower [1,2]. Flow batteries (FBs), which consist of two circulating (positive and negative) redox couples stored in external electrolytes, can offer a long lifespan exceeding 20 years with over 20,000 charge cycles, and superior safety. State-of-the-art technology, vanadium flow batteries (VRBs), suffer from limited availability and high cost of vanadium which hinders their wide-scale commercialization. Recently, numerous studies have focused on the development of new materials, with organic materials in particular showing some promise [3,4]. Properties of the organic molecules can be tuned by functionalization, which affects solubility, stability and redox potential, and molecules can also be designed to be operated in alkaline, neutral and acidic conditions [5]. The energy density limitation associated with aqueous organic flow batteries (AOFBs) in comparison to vanadium is mainly dependent on the lower solubility of the organic materials in the electrolyte - it is not an inherent property of organic redox-active species [6,7]. Among the various organic candidates, quinone derivatives have emerged as one of the most promising classes for use in aqueous FBs. Quinones as a class of metal-free organic compounds are naturally abundant and can undergo reversible redox reactions involving two-electron and two-proton transfers under acidic conditions [8]. They have tunable redox potentials and can be easily converted into water-soluble derivatives using a low-cost starting structure [9,10]. Benzoquinone, naphthoquinone and anthraquinone have been extensively investigated, particularly in alkaline AOFBs [11–13]. Anthraquinone-2,7-disulfonic acid (AQDS) paired with $Br_2$ was one of the earliest reported derivatives, showing a

* Corresponding authors at: Department of Chemistry and Materials Science, Aalto University, Finland.
** Correspondence to: P.M. Pihko, University of Jyväskylä, Finland.
*E-mail addresses:* Chanez.maouche@aalto.fi (C. Maouche), Petri.pihko@jyu.fi (P.M. Pihko), Pekka.peljo@aalto.fi (P. Peljo).
[1] Equal contribution

https://doi.org/10.1016/j.est.2026.122025
Received 13 January 2026; Received in revised form 9 March 2026; Accepted 30 March 2026
Available online 8 April 2026

capacity fade rate of 0.9% per day [14]. While, 2,7-AQDS prepared together with other electroactive compounds (2,6-AQDS and 2-AQS) demonstrated a significantly higher capacity fade of 6% per day [15], in addition of a high-power density of 0.6 W $cm^{-2}$ at 1.3 A $cm^{-2}$ in a single cell. This performance is attributed to the redox couple's high aqueous solubility (>1 M), low crossover rate, and good charge retention. However, the use of $Br_2$ presents challenges due to its volatility, corrosiveness, and safety concerns, which may limit its practical deployment in large-scale or long-term applications [16]. Hydroxyl-modified quinone derivatives such as 2,5-dihydroxybenzoquinone and 2,6-dihydroxyanthraquinone have been studied in alkaline electrolytes, but they suffer from rapid degradation, with a capacity fade rate exceeding 3% per day [17]. These derivatives are in general less suitable for acidic environment [17]. So far, to the best of our knowledge, only few AOFB system using organic material at kW-class has been reported [19][40]. Kwon et al. used 2,7-AQDS as the negolyte and vanadium oxide sulfate ($VOSO_4$) as the posolyte, and they further added manganese to control the osmotic pressure of the active material to suppress their crossover and increase their reactivity[19]. However, the limited solubility and the crossover of the active materials remain the major challenge of their work although the $MnSO_4$ additive effectively reduced the vanadium crossover and further limited reduction of osmotic gaps. Zhang et al. reported a kW class methylene blue/vanadium flow battery [40]. In general, quinones suffer from low solubility and stability issues. Their solubility is often pH-dependent and decreases at neutral pH. While acidic or basic conditions can enhance the solubility, they may also lead to lower stability through reactions such as epoxidation, nucleophilic attack, dimerization, and tautomerization [20]. To overcome the stability and solubility limitations of quinone derivates, one of the promising approaches involves the integration of charged functional groups directly into the aromatic ring of the anthraquinone to improve water solubility while maintaining redox reversibility.

Herein, we present a molecular design strategy that introduces a nitrogen-based cationic group into the anthraquinone framework, to enhance the aqueous solubility, molecular stability and redox tunability through electronic modulation. In this study, AAQ-1 as a negolyte, demonstrated a good solubility of 847 mM within two electron-transfer processes (equivalent of 1.69 M of transferable electrons) in 2 M $H_2SO_4$. At a low battery concentration of 5 mM AAQ-1 exhibited good cycling stability over 480 cycles, with average discharge capacity fade of 0.02% per cycle and 0.74% per day. Moreover, at a high concentration of 500 mM, the system achieved a coulombic efficiency of 100%, indicating highly efficient charge storage and transfer. In addition, a small decay is only observed after 57 days, with a decay of 0.05% per day (0.01% per cycle) and reached 380 mAh at cycle 270, close to the theoretical capacity of 402 mAh.

## 2. Design of the negolytes

In the field of AOFBs, anthraquinones are typically designed with an external hydrophilic group such as sulfonate for AQDS. Here, our strategy involved the replacement of this hydrophilic group by a quaternized pyridinium ring in the anthraquinone core (see Scheme 1A). We selected 5,8-difluoro-2-aza-anthraquinone as starting material due to commercial availability. Also, this compound bears two fluorine atoms that are suitable for nucleophilic aromatic substitution, offering exciting opportunities for molecular engineering. Finally, the pyridine ring enables alkylation reactions to form pyridinium salts. This modification can enhance solubility and redox activity, as demonstrated in previous studies (see Scheme 1B). In this work, we decided to focus on the functionalization of nitrogen.

To functionalize the aza-anthraquinone core, *N*-alkylation of 5,8-difluoro-2-aza-anthraquinone with various electrophiles proceeded readily in dimethylformamide (DMF), resulting in a series of pyridinium salts (AAQ-1, AAQ-2, and AAQ-3) in reasonable yields ranging from 52% to 85%. (Scheme 2). The synthesis can be scaled up to multigram scale (for details, see the Supporting Information).

## 3. Results and discussion

### 3.1. Electrochemical studies

The study started by examining aza-anthraquinones AAQ-1, AAQ-2 and AAQ-3. We initially explored the electrochemical behavior of the

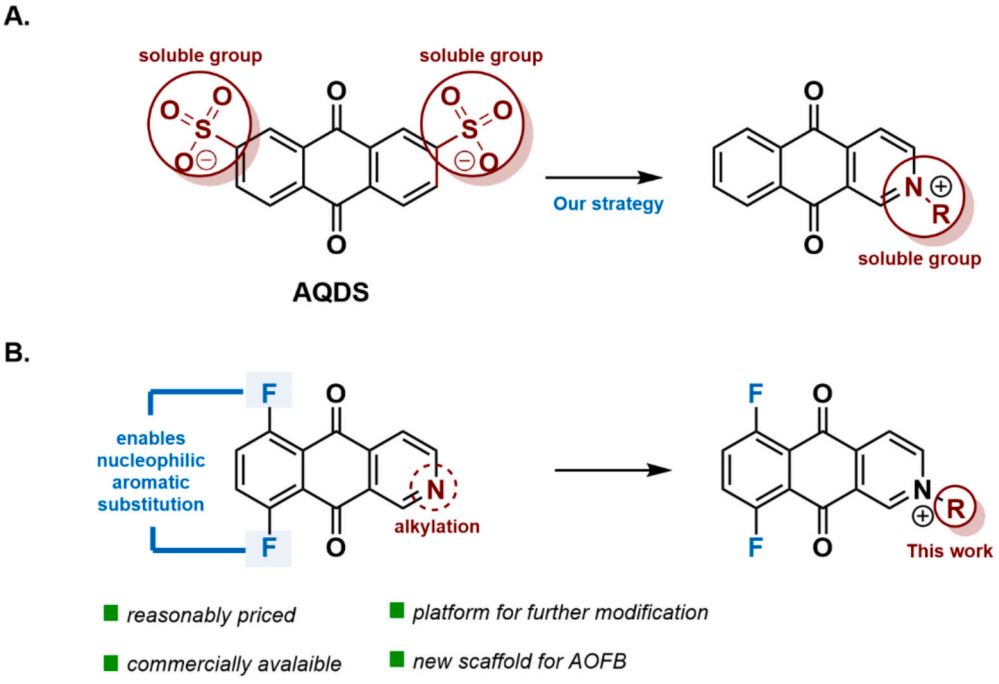


**Scheme 1.** A. Strategy to use the pyridinium cation as the solubility-enhancing group instead of sulfonate. B. Advantages of 5,8-difluoro-2-aza-anthraquinone as a core structure for AOFBs.

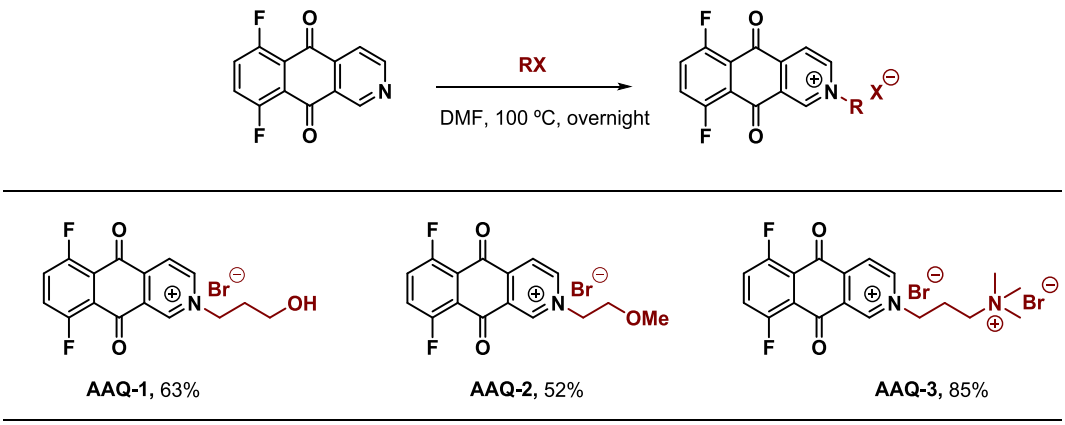


**Scheme 2.** Scope of the *N*-alkylation of 5,8-difluoro-2-aza-anthraquinone

redox material at a concentration of 1 mM in a nitrogen ($N_2$)-saturated 0.1 M $H_2SO_4$ solution, using cyclic voltammetry (CV). All the prepared compounds exhibited a pair of redox-reversible peaks as shown in Fig. 1. The equilibrium potentials were mainly located at 0.083 V vs. Ag/AgCl for AAQ-1, at 0.124 V vs. Ag/AgCl for AAQ-2, and at 0.088 V for AAQ-3 vs. Ag/AgCl. Furthermore, CVs of AAQ derivatives at different scan rates (Figurers S1a-S3a) show that the peak current increases progressively with scan rates while AAQ-1 exhibited a consistent peak shape with no abnormalities. To assess the underlying charge transport mechanism, the CV responses were normalized as $i/\upsilon^{1/2}$ (Figs. S1b–S3b). The overlap of the normalized curves together with log($i_p$) vs. log(υ) slopes close to 0.5 (Fig. S1c-S3c) suggests a predominantly diffusion-controlled redox process, in line with the Randles-Ševčík relationship [21] as the current did not change significantly between scan rates from 5 mV/s to 100 mV/s. However, when the scan rates are increased to 500 mV/s the current increase while compared to lower speed, suggesting diffusion controlled process together with weak adsorption [22].

### 3.2. Rotating disk electrode studies

The diffusion coefficient ($D$) and the kinetic reaction rate constant ($k^0$) were investigated using linear sweep voltammetry (LSV) to understand the electrochemical polarization properties of AAQ-1 molecule [23]. Larger values of $D$ and $k^0$ indicate lower resistance to mass transfer and charge transfer. LSV curves were collected at multiple rotation rates (200–3600 r.p.m., Fig. 2a).

The diffusion coefficient of AAQ-1 was calculated using the Levich equation:

$$i_p = 0.620nFAC_OD^{2/3}\,\nu^{-1/6}$$

where $i_p$ is the mass-transport limited current, $n$ is number of electrons transferred ($n = 2$), the Faraday constant ($F$) was taken as 96,485C/mol, $A$ is the working electrode area ($A = 19.635$ mm$^2$), $C_O$ is concentration of redox-active species in the electrolyte ($C_O = 1$ mM), and the kinematic viscosity of the electrolyte (0.1 M $H_2SO_4$) was taken as $\nu = 1.005 \times 10^{-6}$ m$^2$/s.

The mass-transport-limited current was plotted against the square

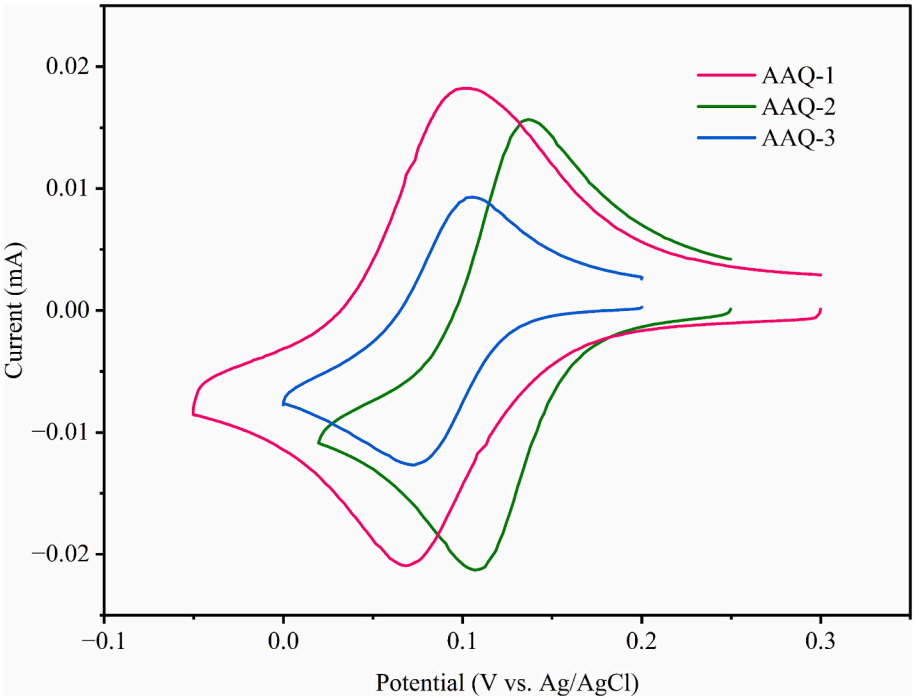


**Fig. 1.** CV curves of AAQ derivatives in 0.1 M $H_2SO_4$, at a scan rate of 100 mV/s.

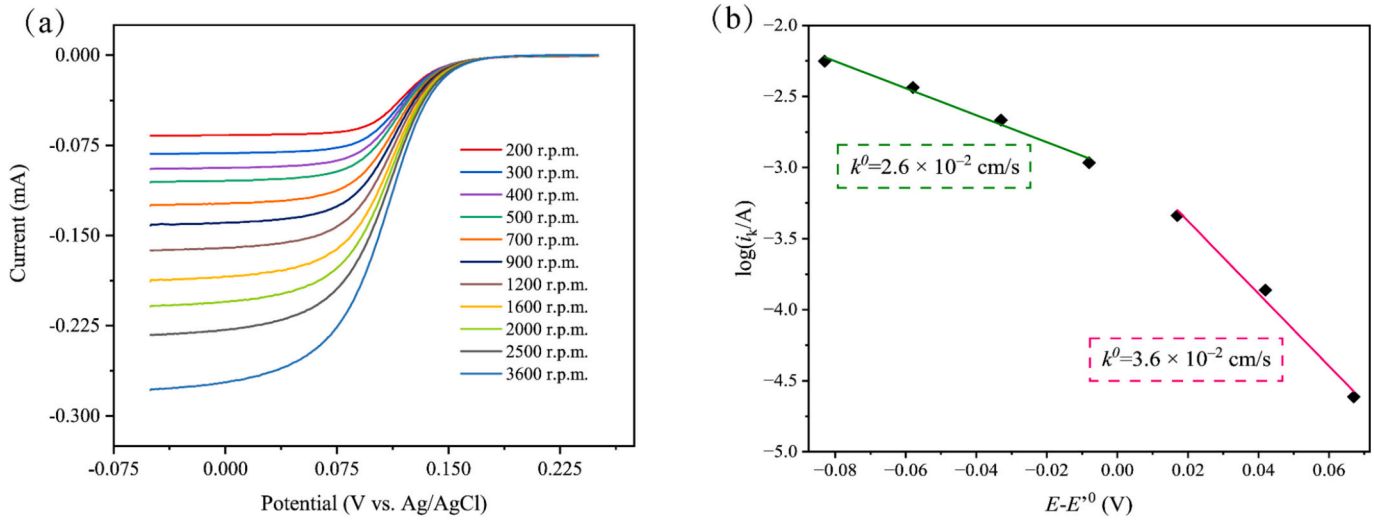


**Fig. 2.** (a) Rotating disk electrode (RDE) measurements of AAQ-1 in 0.1 M $H_2SO_4$ at rotation rates ranging from 200 to 3600 r.p.m. (b) Linearly fitted plots of log($i_k$) versus $E - E^{'0}$ ($E^{'0}$ = 0.083 V vs. Ag/AgCl).

root of the rotation rate (Fig. S4a). The *D* of AAQ-1 was determined to be $4.75 \times 10^{-6}$ $cm^2$ /s, higher than that of those reported anthraquinone-based electrolytes in $H_2SO_4$ (Table S9) such as AQDS ($3.8 \times 10^{-6}$ $cm^2$/s) [24] and 2,7-AQDS ($2.26 \times 10^{-7}$ $cm^2$/s) [19]. In addition, the Koutecký-Levich (K-L) plot reveals a good linearity of reciprocal electrode currents against the reciprocal square root of rotation rate at different overpotentials (Fig. S4b). The Fitting of the kinetically limited current $i_k$ to the Tafel equation (Fig. 2b) yields a transfer rate constant ($k^0$) from $2.6 \times 10^{-2}$ cm/s to $3.6 \times 10^{-2}$ cm/s [25], exceeding those of other quinone derivatives, including Phoenicin ($1.56 \times 10^{-4}$ cm/s) [26] and 2,7-AQDS ($5.73 \times 10^{-5}$ cm/s) [19] in 1 M KOH and 0.1 M $H_2SO_4$ respectively. Moreover, the kinetic rate constant of AAQ-1 is greater than the common redox species in FB including $Fe^{3+}/Fe^{2+}$ ($1.5 \times 10^{-3}$ cm/s) [27] and $V^{3+}/V^{2+}$ (from 1 to $4 \times 10^{-3}$ cm/s) in acidic media [28].

### 3.3. UV–Vis spectroscopy

The maximum solubility of AAQ-1 in 2 M $H_2SO_4$ was determined by UV–Vis spectroscopy using calibration curves at two characteristic wavelengths (295 and 369 nm, Fig. S5). The saturated AAQ-1 solution corresponds to 834 mM (295 nm) and 859 mM (369 nm), giving an average solubility of 847 mM. Under the same condition (as shown in Fig. S6), AAQ-3 is far less soluble, giving 45 mM (271 nm) and 57 mM (292 nm). The corresponding average solubility of AAQ-3 is 51 mM. The introduction of a hydroxyl group in AAQ-1 favorably affects solubility by increasing the hydrophilicity of the molecule and improving it through hydrogen-bonding interactions with water [29,30]. AAQ-2 and AAQ-3 showed poor solubility in acidic media, with visible undissolved particles in the electrolyte solutions. The significantly lower solubility of AAQ-3 compared to AAQ-1 may arise from differences in the hydrophilicity of the side chain substituent rather than electronic effects. AAQ-1 contains an OH group that can hydrogen bond with water, enhancing solvation. In contrast, AAQ-3 lacks hydrogen-bond donating functionality and has a more hydrophobic alkyl character, which promotes aggregation and limits solubility in acidic media. The methyl ether group in AAQ-2 cannot act as a hydrogen bond donor, which may reduce its solubility compared to AAQ-1. Overall, the observed solubility trend correlates more strongly with polarity and hydrogen-bonding ability than with electronic effects [32]. We note, however, that solubilities of organic compounds can sometimes be very difficult to predict due to the possibility of different polymorphs and intermolecular contacts.

### 3.4. pH dependence

The relation between the redox potential and pH was investigated to elucidate the mechanism of the redox process of AAQ-1 (Fig. 3a-3b). Britton-Robinson buffer (BRB) was used to perform CV at different pH, using a low concentration of 1 mM AAQ-1 as shown in Fig. 3a, and the data was utilized to construct a Pourbaix diagram in Fig. 3c. The pH was adjusted with diluted NaOH. In BRB the redox peak shifted by 60 mV per unit of pH at low pH from 1.90 to 3 and then by 30 mV per unit of pH. As the pH is increasing toward near-neutral conditions, the redox peak remained constant, while a small oxidation peak appeared, indicating a change in the redox mechanism or the formation of new species. Furthermore, a visible color change of the solution was observed, shifting from yellow to brown at higher pH. In addition, pH can influence the chemical stability of anthraquinone derivatives. Previous studies have shown that one of the primary pathways for capacity fade in anthraquinone systems is anthrone dimerization, which is strongly affected by the pH of the electrolyte [33,34]. These findings give an insight into pH-dependent redox behavior of AAQ-1. The related potentials yield a slope of 54 mV/pH in $H_2SO_4$, at pH 0, and a slope of 60 mV/pH at pH from 1.97 to 3.04. Moreover, the Pourbaix diagram in Fig. 3c confirms a pH-dependent redox equilibrium, suggesting a proton coupled electron transfer (PCET) reaction [35,36]. This indicates a $2e^-/2H^+$ electron transfer mechanism, as expected for quinones [37,38]. Above pH 3 the reduced AAQ-1 becomes deprotonated, resulting in the slope of ca. 31 mV/ pH and $2e^-/H^+$ mechanism.

### 3.5. Battery application at low concentration

To establish the stability of AAQ-1, AAQ-2 and AAQ-3, experiments in lab-scale FBs were conducted. The initial stability tests involved galvanostatic cycling using 5 mM of the redox material dissolved in acidic media of 2 M $H_2SO_4$. An excess amount of a mixture of $V^{4+}$and $V^{5+}$ species was used as the posolyte, to ensure that the negolyte is the capacity-limiting side (20 mL of 50 mM $V^{4+}/V^{+5}$ versus 15 mL of 5 mM AAQ) (see Supporting Information). The vanadium-based posolyte ($V^{4+}/V^{5+}$) was selected as a stable and well-established reference catholyte in acidic media, as demonstrated in vanadium flow batteries (VFBs). Its high electrochemical reversibility and stability make it a suitable benchmark catholyte in sulfuric acid. The cell was assembled using a Selemion DSVN anionic exchange membrane and we performed all the tests inside a $N_2$-filled glovebox. The theoretical capacity of the three compounds was calculated to be 4.02 mAh. Fig. 4 presents the

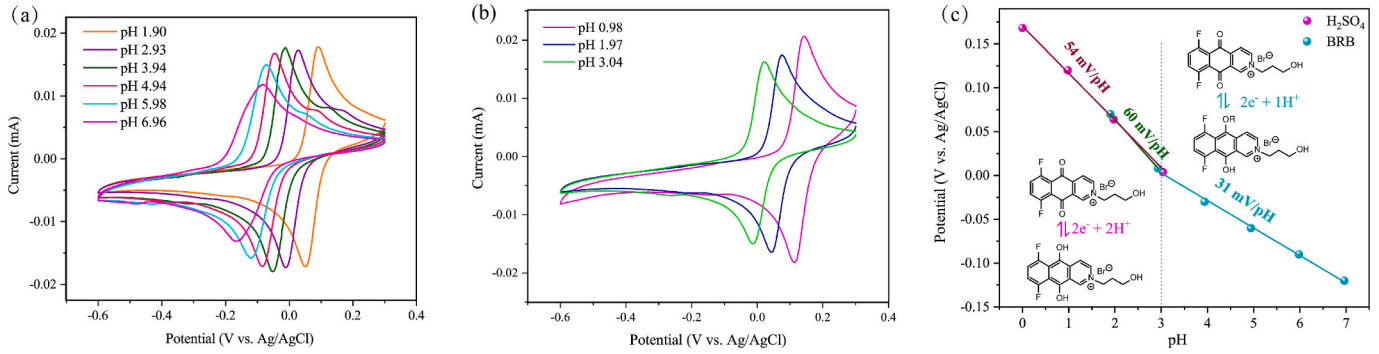


**Fig. 3.** (a) CV curves of AAQ-1 at different pH values and at scan rate of 100 mV/s in BRB. (b) CV curves of AAQ-1 at different pH values and at scan rate of 100 mV/s in 0.1 M $H_2SO_4$. (c) Pourbaix diagram of AAQ-1 from Figure (a) and (b), the pH ≈ 0 data point was taken from the CV in 2 M $H_2SO_4$ (Fig. 5a).

cycling performance of batteries with AAQ-1, AAQ-2 and AAQ-3. AAQ-1 (Fig. 4a) exhibited good cycling stability over 480 cycles, as its discharge capacity decreased only from 2.998 mAh to 2.713 mAh, corresponding to an average capacity fade of 0.02% per cycle and 0.74% per day. A protocol adjustment at cycle 148 (increasing the constant-voltage (CV) cut-off current from 1 mA to 2.5 mA) contributed to the observed improvement in coulombic efficiency (CE) and energy efficiency (EE) around cycle ~150 (see SI Fig. S7 for details on CV phase durations). The average CE and EE remained at 97.7% and 89.9%, respectively, indicating stable electrochemical performance.

In contrast, AAQ-2, as shown in Fig. 4b, exhibited a higher initial capacity (3.673 mAh); however, it underwent degradation, decreasing to 3.547 mAh after only 60 cycles, with an average capacity fade of 0.06% per cycle and 0.93% per day. While AAQ-2 showed a slightly lower CE of 97.2%, it achieved a higher EE 93.5%, suggesting better energy conversion efficiency but worse long-term cycling stability. AAQ-3 (Fig. 4c), on the other hand, with an initial capacity of 2.921 mAh, remained 2.767 mAh after 480 cycles, exhibiting a 0.01% per cycle capacity fade (0.46% per day), which is slightly more stable than AAQ-1. Additionally, it maintains a higher CE of 99.2% and EE of 90.7%. We also analyzed the representative galvanostatic charge–discharge voltage–capacity profiles for the low-concentration cells. The observed profile evolution is consistent with the cycling trends discussed above; further details are provided in the SI, Section 10. Overall, AAQ-1 and AAQ-3 demonstrate superior long-term stability, whereas AAQ-2 exhibits 1.5 to 2 times faster capacity degradation. One hypothesis could be that the side-chain length is shorter, but confirming this would require further studies.

### 3.6. Post-mortem analysis of 5 mM of AAQ-1 battery

After cycling, AAQ-1 battery was stopped and disassembled to examine the behavior of the electrolytes. CV was performed on both AAQ-1 negolyte and vanadium posolyte under $N_2$ atmosphere prior and after battery testing (Fig. 5a and Fig. 5b). Before the battery testing, a redox peak was observed for the negolyte at 0.2 V. After battery testing, the CV was conducted on the discharged electrolytes immediately after disassembling the cell outside the glovebox to minimize contamination. CVs of the negolyte and posolyte (Fig. 5) show no crossover of AAQ-1. A weak feature at 1.5 V, consistent with the $V^{4+}/V^{5+}$ couple, indicates slight vanadium crossover. CVs of the negolyte and the corresponding vanadium posolyte from the AAQ-2 and AAQ-3 full cells were recorded in 2 M $H_2SO_4$ before and after cycling (Fig. S9). AAQ-2 shows a positive shift of the negolyte redox peaks after cycling, whereas AAQ-3 displays a response similar to AAQ-1, with a weak vanadium-related feature appearing in the negolyte consistent with minor vanadium crossover.

To quantify active-material crossover beyond qualitative inference from post-mortem CV, we measured the membrane permeability of the AAQ series across Selemion DSVN using a side-by-side diffusion cell (Fig. S10). Under identical conditions, AAQ-2 shows the highest permeability ($1.06 \times 10^{-8}$ $cm^2/s$) among the three derivatives, AAQ-1 exhibits a permeability of ($9.64 \times 10^{-10}$ $cm^2/s$), while AAQ-3 demonstrates the lowest permeability ($3.70 \times 10^{-10}$ $cm^2/s$). This indicates that AAQ-3 is retained most effectively by DSVN, whereas AAQ-2 is most prone to transmembrane transport under the same conditions. This can be explained by AAQ-3 having a total charge of +2, while the others have charge of +1, resulting in stronger repulsion by the anion exchange membrane. AAQ-2 has a side chain of 2 carbons, indicating that the size is smaller, leading to higher permeability.

### 3.7. High concentration battery

In a full cell, 15 mL of 500 mM of AAQ-1 was investigated as the negolyte, and an excess of 100 mL of 1.6 M of vanadium electrolyte as the posolyte. 2 M $H_2SO_4$ was used as the supporting electrolyte and DSVN as the membrane. The battery was cycled in a $N_2$-filled glovebox at room temperature (25 °C). At the beginning of cycling, the cell operated with a cut-off voltage of 0.4 V to 0.8 V and a current density of 20 mA $cm^{-2}$. At 4th cycle, the current density was increased to 30 mA $cm^{-2}$ while maintaining a constant flow rate of 30 mL $min^{-1}$. Subsequently, at 25th cycle, the cut-off voltage was raised to 0.85 V, as shown in Fig. 6a. The voltage-time profiles at the beginning of the test are shown in Fig. S11. Within this potential window, the battery was unable to achieve full charge due to ion transport limitations, leading to a noticeable decrease in capacity. However, when a higher cut-off potential was applied, the battery underwent complete charge-discharge cycles, allowing the capacity to recover and stabilize. On the other hand, voltage efficiency of the battery decreased significantly between 1st and 50th cycle but then remained constant. This excludes decreasing resistance, improved kinetics etc. as the reason for the change in the accessed capacity. An average CE was 99.65% throughout the testing period, indicating efficient charge storage and transfer (Fig. 6b). In addition, a capacity increase is observed during cycling. The capacity increase can be attributed to the battery not fully utilizing its storage potential during the early cycles, with performance gradually improving over time. Moreover, the electrolyte volume decreased over time. As the tank was not stirred, it is possible that there was some stagnation in the tank. As the volume decreased while the pumping rate remained constant, this would improve the mixing in the tank, leading to full capacity utilization. Furthermore, during cycling, the battery demonstrated excellent stability with a volumetric capacity of 25.6 Ah/L under standard conditions, without significant fading capacity until cycling 57 days, where a small decay of 0.01% per cycle and 0.05% per day is observed. The capacity continued to increase and stabilized around 380 mAh after 52.5 days, approaching the theoretical value of 402 mAh. Notably, if the highest electrolyte concentration (847 mM) were used, the battery could theoretically reach the maximum volumetric capacity of 43.4 Ah/L. The overall result of the battery highlights the robustness

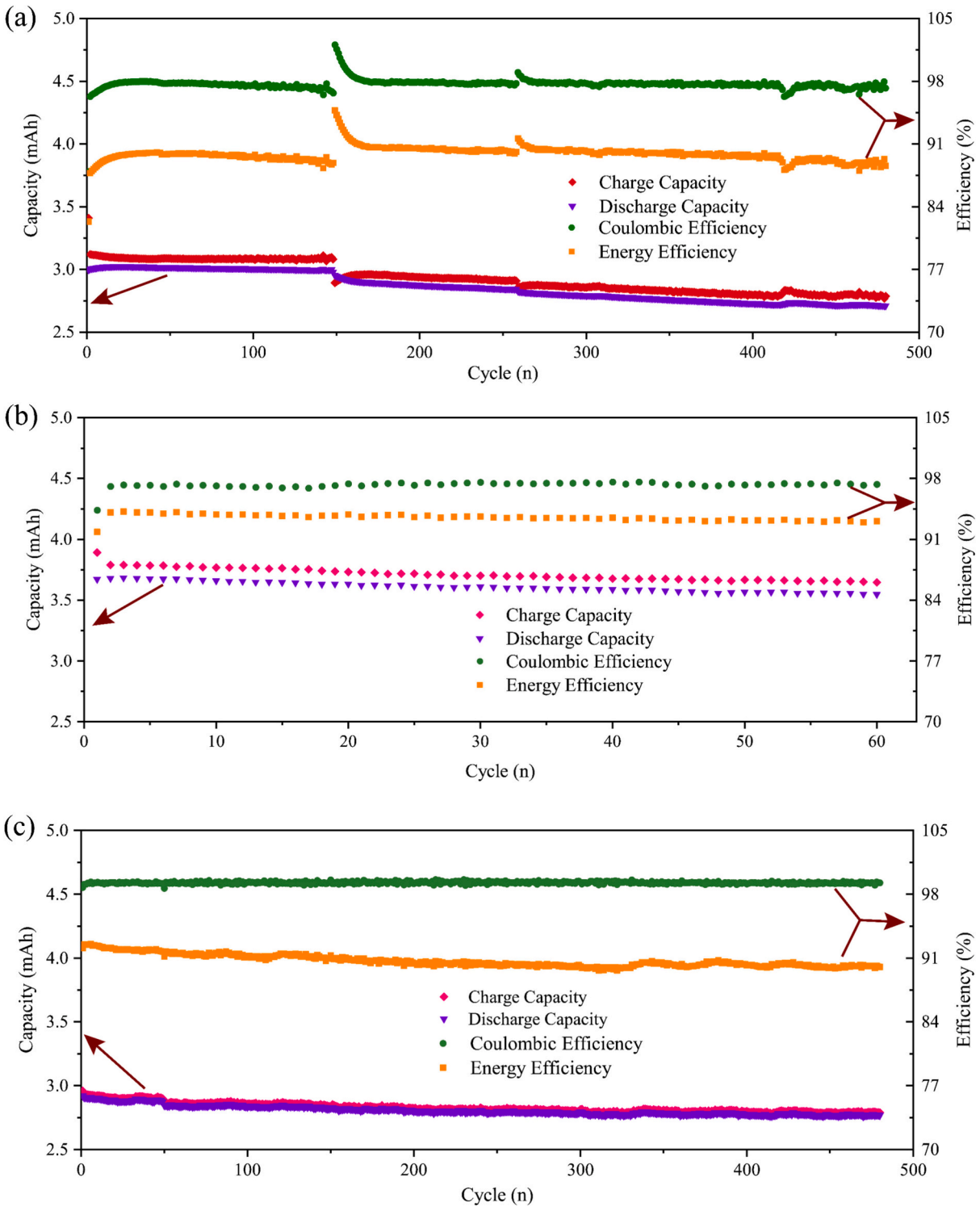


**Fig. 4.** Full cell performance of different compounds at 5 mM in 2 M $H_2SO_4$. (a) AAQ-1, (b) AAQ-2, and (c) AAQ-3.

of our design, suggesting that optimizing the electrolyte concentration can play a crucial role in enhancing the battery's performance while ensuring long-term stability.

### 3.8. Post mortem

Fig. 7 presents the UV–Vis absorption spectra of 0.1 mM AAQ-1 in 2 M $H_2SO_4$ before and after battery cycling. It was observed that the major absorption peaks remain unchanged, indicating a high structural stability of the compound during cycling. Although the peak positions are consistent, the absorption intensity increases after cycling. The increased absorbance is attributed to the reduction in solution volume from 15 mL to 9.5 mL, which resulted in a higher concentration of the compound. The reduction of the volume can be attributed to water transfer across the membrane driven by osmotic pressure difference between the two half cells, in addition to evaporation during the long cycling. The absence of new peaks after battery cycling gives further confirmation that the compound has good chemical and structural

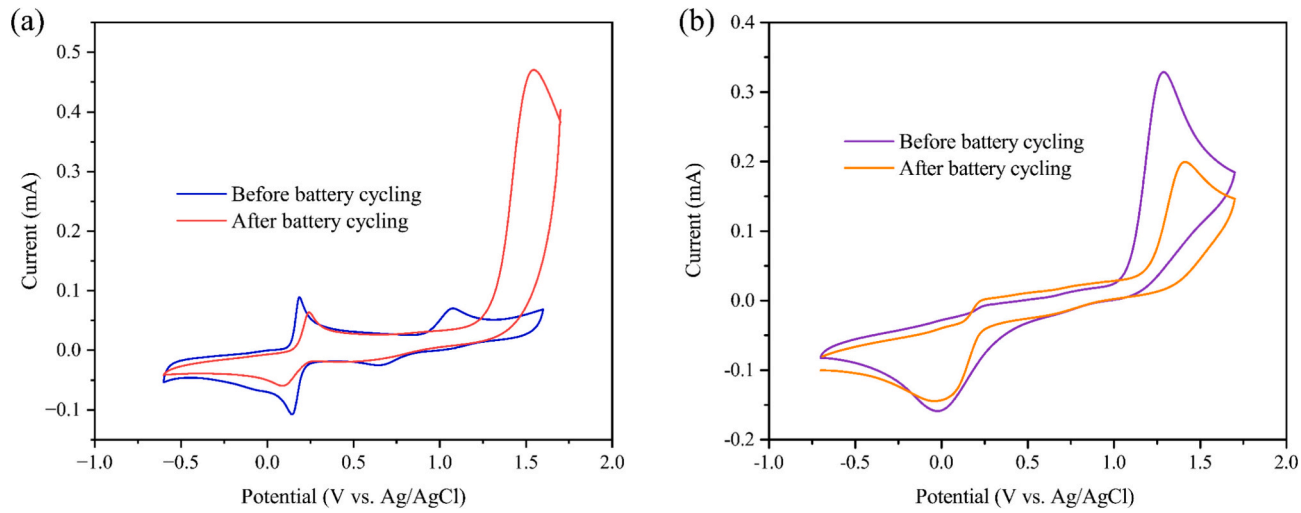


**Fig. 5.** CV curves of the AAQ-1 and vanadium electrolyte in 2 M $H_2SO_4$ before and after full cell cycling. (a) AAQ-1 at a concentration of 5 mM. (b) Vanadium electrolyte at a concentration of 100 mM. The scan rate was 100 mV/s for both measurements.

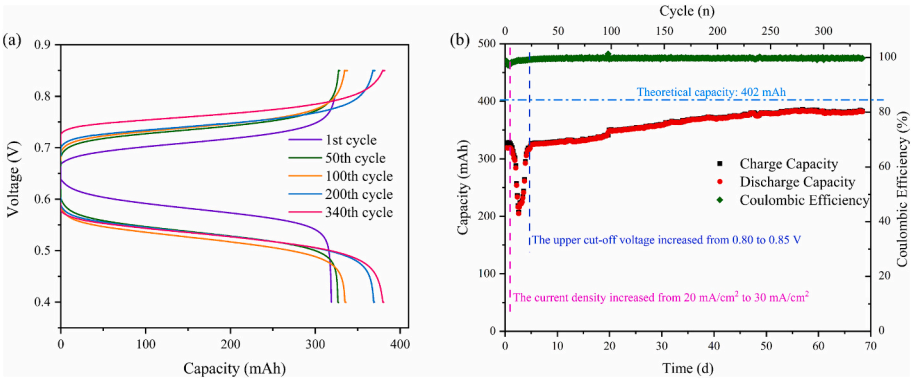


**Fig. 6.** AAQ-1 full cell (500 mM) performance in a two-electron cycling experiment. (a) Capacity and voltage curves at different cycles. (b) Capacity and coulombic efficiency performance over 70 days of cycling.

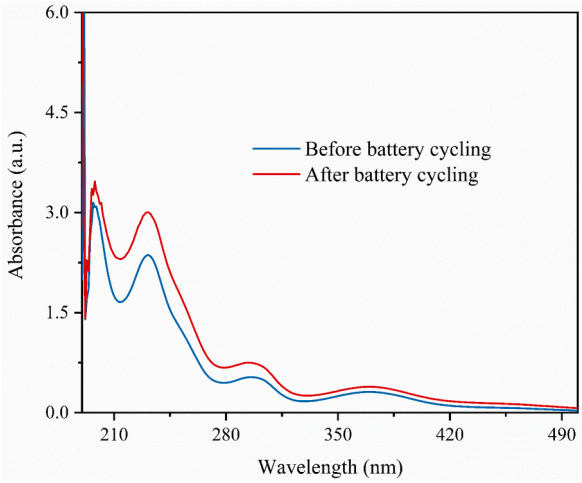


**Fig. 7.** UV–Vis spectra of the AAQ-1 in 2 M $H_2SO_4$ before and after battery cycling. The original electrolyte concentration was 500 mM, but due to the high absorbance at this level, electrolyte was diluted to 0.1 mM prior to measurement.

stability. The electrochemical performance of the battery before and after cycling was investigated using CV (Fig. S12), confirming that the material retains electrochemical activity after cycling.

## 4. Conclusion

A rational molecular strategy for AOFBs based on the functionalization of aza-anthraquinones with quaternized pyridinium groups was successfully designed using 5,8-difluoro-2-aza-anthraquinone as a raw material. The efficient N-alkylation protocol yielded a new class of redox-active pyridinium salts. This approach enhances both solubility and redox performance through electronic modulation, while offering an affordable synthesis and structural tunability. Also, the presence of two fluorine atoms provides excellent opportunities for further molecular tailoring. The AAQ-1 derivative demonstrated good electrochemical properties, including high solubility (average 847 mM in 2 M $H_2SO_4$), a fast electron transfer rate ($k^0 = 2.6 \times 10^{-2}$ cm/s), and a diffusion coefficient ($D = 4.75 \times 10^{-6}$ $cm^2/s$) matching that of benchmark anthraquinones in acidic media (2,7-AQDS $3.80 \times 10^{-6} cm^2/s$) [24] but also in alkaline media (DHBQ $3.66 \times 10^{-6}$ $cm^2/s$) [9]. The flow cell testing at a concentration of 5 mM, for all the prepared AAQ derivatives demonstrated a capacity fade below 0.06% per cycle (0.93% per day), which is lower than the reported 2.7-AQDS [24] in $H_2SO_4$ with a decay of 0.78% per cycle, noting that only few studies have been demonstrated in acidic media. For comparison, a reported a series of phenazine derivatives with improved chemical stability, based on benzo [*a*]hydroxyphenazine-7/8-carboxylic acid demonstrated a low capacity fade rate of 0.08% per day [39]. However, both DHPS and BHPC systems

were operated under strongly alkaline conditions. In contrast, stability and operability in acidic environments remain less explored for phenazine-based systems, where challenges such as molecular degradation and compatibility may arise. Moreover, AAQ-1 reached a capacity of 380 mAh after 52.2 days, approaching the theoretical capacity of 402 mAh, and delivered a volumetric capacity of 25.6 Ah/L, approaching 43.4 Ah/L theoretically. Furthermore, Pourbaix analysis validated a $2e^-/2H^+$ PCET mechanism for the redox cycle, supporting robust redox activity over an acidic pH range. This work highlights the potential of pyridinium-functionalized quinones as scalable and tunable negolyte materials for high-performance, long-duration energy storage and demonstrates competitive long-term performance in this class of material. The combined strategy of synthetic modification of the core structures and electrochemical engineering paves the way toward next-generation AOFB systems with improved stability, capacity, and design flexibility.

## CRediT authorship contribution statement

**Qiujun Li:** Writing – original draft, Visualization, Methodology, Investigation, Formal analysis, Writing – review & editing. **Maxime Artault:** Writing – original draft, Visualization, Methodology, Investigation, Formal analysis, Conceptualization, Writing – review & editing. **Chanez Maouche:** Writing – original draft, Visualization, Methodology, Investigation, Formal analysis, Writing – review & editing. **Gabriel Gonzalez:** Formal analysis, Methodology. **Petri M. Pihko:** Writing – review & editing, Supervision, Resources, Funding acquisition, Conceptualization. **Pekka Peljo:** Writing – review & editing, Validation, Supervision, Resources, Conceptualization.

## Declaration of competing interest

The authors declare that they have no known competing financial interests or personal relationships that could have appeared to influence the work reported in this paper.

## Acknowledgments

Support from Research Council Finland (project 348328 – via European Union – NextGenerationEU instrument – to P. M. P. and 348326 to P.P.) is gratefully acknowledged. G.G. gratefully acknowledges the financial support from the University of Turku Graduate School. Materials Analysis and Research Infrastructure (MARI) of the University of Turku was utilized in this work.

## Appendix A. Supplementary data

Supplementary data to this article can be found online at https://doi.org/10.1016/j.est.2026.122025.

## Data availability

Data will be made available on request.

## References

[1] C. Maouche, Y. Zhou, B. Li, et al., A stabilized assisted method for the synthesis of Fe-N-C catalysts for the oxygen reduction reaction, J. Electrochem. Soc. 169 (6) (2022) 062501, https://doi.org/10.1149/1945-7111/ac7260.
[2] J. Rugolo, M.J. Aziz, Electricity storage for intermittent renewable sources, Energy Environ. Sci. 5 (5) (2012) 7151–7160, https://doi.org/10.1039/c2ee02542f.
[3] J. Cui, Z. Liu, C. Song, et al., Optimizing Zn-Mn flow batteries with aminonaphthalene sulfonic acid via hydrogen bond disruption and interface, Small (2025), https://doi.org/10.1002/smll.202506034. Art no. 2506034.
[4] P. Navalpotro, A. Mavrantonakis, R. Marcilla, Unraveling the role of supporting electrolytes in organic redox flow battery performance, J. Energy Storage 131 (2025), https://doi.org/10.1016/j.est.2025.117570. Art no. 117570.
[5] E.M. Fell, M.J. Aziz, High-throughput electrochemical characterization of aqueous organic redox flow battery active material, J. Electrochem. Soc. 170 (10) (2023) 100507, https://doi.org/10.1149/1945-7111/acfcde.
[6] M. Pan, M. Shao, Z. Jin, Development of organic redox-active materials in aqueous flow batteries: current strategies and future perspectives, SmartMat 4 (2023) e1198, https://doi.org/10.1002/smm2.1198.
[7] M. Ulaganathan, V. Aravindan, Q. Yan, et al., Recent advancements in all-vanadium redox flow batteries, Adv. Mater. Interfaces 3 (1) (2016), https://doi.org/10.1002/admi.201500309.
[8] J.-M. Fontmorin, S. Guiheneuf, T. Godet-Bar, et al., How Anthraquinones can enable aqueous organic redox flow batteries to meet the needs of industrialization, Curr. Opin. Colloid Interface Sci. 61 (2022), https://doi.org/10.1016/j.cocis.2022.101624.
[9] Z. Yang, L. Tong, D.P. Tabor, et al., Alkaline benzoquinone aqueous flow battery for large-scale storage of electrical energy, Adv. Energy Mater. 8 (8) (2018) 1702056, https://doi.org/10.1002/aenm.201702056.
[10] M. Park, E.S. Beh, E.M. Fell, et al., A high voltage aqueous zinc–organic hybrid flow battery, Adv. Energy Mater. 9 (25) (2019) 1900694, https://doi.org/10.1002/aenm.201900694.
[11] S. Singh, J.L. Tami, C. Gruich, et al., Sulfonated benzo[c]cinnolines for alkaline redox-flow batteries, ACS Appl. Energy Mater. 8 (12) (2025), https://doi.org/10.1021/acsaem.4c02861, 2025/06/04.
[12] P. Zhang, Y. Liu, J. Wei, et al., An amphoteric and hydrogen-bond-rich artificial α-amino acid for highly durable aqueous redox flow batteries, Nat. Commun. 16 (2025) 4727, 2025/05/21, https://doi.org/10.1038/s41467-025-59962-1.
[13] T. Murata, M. Hamasaki, Y. Morita, A benzoquinone–imidazole hybrid organic Anolyte for aqueous redox flow batteries, Chem. Commun. 60 (7) (2024) 2024, https://doi.org/10.1039/D3CC04840C.
[14] P. Mazúr, J. Charvát, J. Mrkl, et al., Evaluation of electrochemical stability of sulfonated anthraquinone-based acidic electrolyte for redox flow battery application, Molecules 26 (9) (2021) 2484, 2021/04/24, https://doi.org/10.3390/molecules26092484.
[15] M.M. Petrov, D.V. Chikin, K.A. Karpenko, et al., Tuning the composition of mixed Anthraquinone derivatives towards an affordable flow battery Negolyte, J. Electroanal. Chem. 973 (2024) 118693, 2024/11/15, https://doi.org/10.1016/j.jelechem.2024.118693.
[16] T. Luyin, L. Wenjing, Z. Huamin, et al., Progress and perspective of the cathode materials towards bromine-based flow batteries, Energy Mater Adv 2022 (2022) 9850712, 2022/02/17, 10.34133/2022/9850712.
[17] C. Wang, Z. Yang, Y. Wang, et al., High-performance alkaline organic redox flow batteries based on 2-Hydroxy-3-carboxy-1,4-naphthoquinone, ACS Energy Lett. 3 (2018) 2404–2409, https://doi.org/10.1021/acsenergylett.8b01296.
[19] G. Park, H. Jeong, W. Lee, et al., Scaled-up aqueous redox flow battery using Anthraquinone Negalyte and vanadium Posilyte with inorganic additive, Appl. Energy 353 (2024), https://doi.org/10.1016/j.apenergy.2023.122171.
[20] D.G. Kwabi, Y. Ji, M.J. Aziz, Electrolyte lifetime in aqueous organic redox flow batteries: a critical review, Chem. Rev. 120 (14) (2020) 6467–6489, https://doi.org/10.1021/acs.chemrev.9b00599.
[21] A.J. Bard, L.R. Faulkner, H.S. White, Electrochemical Methods: Fundamentals and Applications, John Wiley & Sons, 2022.
[22] E. Martínez-González, A. Tuna, P. Peljo, Phenoxazine radical as a positive material for neutral pH aqueous flow batteries, ACS Appl. Energy Mater. 8 (10) (2025) 6463–6473, 2025/05/26, https://doi.org/10.1021/acsaem.5c00225.
[23] N. Roznyatovskaya, J. Noack, K. Pinkwart, et al., Aspects of electron transfer processes in vanadium redox-flow batteries, Curr. Opin. Electrochem. 19 (2020) 42–48. February 2020, https://doi.org/10.1016/j.coelec.2019.10.003.
[24] B. Huskinson, M.P. Marshak, C. Suh, et al., A metal-free organic–inorganic aqueous flow battery, Nature 505 (7482) (2014) 195–198, https://doi.org/10.1038/nature12909.
[25] H. Wang, S.Y. Sayed, E.J. Luber, et al., Redox flow batteries: how to determine electrochemical kinetic parameters, ACS Nano 14 (3) (2020) 2575–2584, 2020/03/24, https://doi.org/10.1021/acsnano.0c01281.
[26] C.O. Wilhelmsen, S.B. Kristensen, O. Nolte, et al., Demonstrating the use of a fungal synthesized Quinone in a redox flow battery, Batteries Supercaps 6 (1) (2023), https://doi.org/10.1002/batt.202200365.
[27] J. Weber, Z. Samec, V. Mareček, The effect of anion adsorption on the kinetics of the Fe3+/Fe2+ reaction on Pt and au electrodes in HclO4, J. Electroanal. Chem. Interfacial Electrochem. 89 (2) (1978) 271–288, 1978/05/25/, https://doi.org/10.1016/S0022-0728(78)80190-9.
[28] K. Niki, H. Mizota, Effect of specific adsorbed anions on the electrode kinetics of the V(III)/V(II) and Eu(III)/Eu(II) couples, J. Electroanal. Chem. Interfacial Electrochem. 72 (3) (1976) 307–317, 1976/09/25/, https://doi.org/10.1016/S0022-0728(76)80316-6.
[29] Z. Xiang, W. Li, K. Wan, et al., Aggregation of electrochemically active conjugated organic molecules and its impact on aqueous organic redox flow batteries, Angew. Chem. Int. Ed. Eng. 62 (2) (2023) e202214601. Jan 9, https://doi.org/10.1002/anie.202214601.
[30] Z. Xiang, T. Ren, M. Huang, et al., Manipulating aggregate electrochemistry for high-performance organic redox flow batteries, Angew. Chem. Int. Ed. Eng. 64 (4) (2025) e202416184. Jan 21, https://doi.org/10.1002/anie.202416184.
[32] Y. Liu, K. Wan, Z. Xiang, et al., Full-cycle oxygen-tolerant organic flow batteries, Joule 10 (2) (2026) 102267, 2026/02/18/, https://doi.org/10.1016/j.joule.2025.102267.
[33] F. Fenini, E. Drazevic, A. Bentien, Impact of pH management on utilization and performance of anthraquinone/ ferrocyanide flow batteries, J. Power Sources 540 (2022) 231641, 2022/08/30/, https://doi.org/10.1016/j.jpowsour.2022.231641.

[34] M.A. Goulet, L. Tong, D.A. Pollack, et al., Extending the lifetime of organic flow batteries via redox state management, J. Am. Chem. Soc. 141 (20) (2019) 8014–8019. May 22, https://doi.org/10.1021/jacs.8b13295.
[35] M. Artault, G. Gonzalez, P. Damlin, et al., Azoniafluorenones: a new family of two-electron storage electrolytes for sustainable near-neutral pH aqueous organic flow battery, Adv. Energy Mater. (2024), https://doi.org/10.1002/aenm.202401635.
[36] M. Quan, D. Sanchez, M.F. Wasylkiw, et al., Voltammetry of Quinones in unbuffered aqueous solution: reassessing the roles of proton transfer and hydrogen bonding in the aqueous electrochemistry of Quinones, J. Am. Chem. Soc. 129 (42) (2007) 12847–12856, https://doi.org/10.1021/ja0743083.
[37] C. Wang, B. Yu, Y. Liu, et al., N-alkyl-carboxylate-functionalized Anthraquinone for long-cycling aqueous redox flow batteries, Energy Storage Mater. 36 (2021) 417–426, https://doi.org/10.1016/J.ENSM.2021.01.019.
[38] J. Asenjo-Pascual, I. Salmeron-Sanchez, J.R. Avilés-Moreno, et al., Understanding aqueous organic redox flow batteries: a guided experimental tour from components characterization to final assembly, Batteries 8 (10) (2022), https://doi.org/10.3390/batteries8100193.
[39] C. Wang, X. Li, B. Yu, et al., Molecular Design of Fused-Ring Phenazine Derivatives for long-cycling alkaline redox flow batteries, ACS Energy Lett. 5 (2) (2020) 411–417, 2020/02/14, https://doi.org/10.1021/acsenergylett.9b02676.
[40] Y. Zhang, F. Li, T. Li, et al., Insights into an air-stable methylene blue catholyte towards kW-scale practical aqueous organic flow batteries, Energy Environ. Sci. 16 (2023) 231–240, https://doi.org/10.1039/D2EE03051A.